Multiscale Process Modeling of a Carbon Fiber/Epoxy Composite for Predicting Residual Stress and Strength

Prathamesh P. Deshpande[1], Michael Olaya[2], Aaron Krieg[1], Sagar U. Patil[1], Sagar P. Shah[2], Julia A. King[1], Gregory M. Odegard[1*], Marianna Maiaru[2]

[1]*Michigan Technological University, Houghton, MI 49931*
[2]*University of Massachusetts Lowell, Lowell, MA 01854*

Abstract

During the manufacturing of composite structures, cure shrinkage of the thermoset matrix and differential thermal contraction mismatch between the matrix and fiber reinforcement cause the formation of residual stresses, which can result in a loss in structural durability. New multiscale computational process modeling is essential for linking material chemistry, processing parameters, residual stress evolution, and optimizing mechanical performance. This study establishes a new multiscale process modeling method to accurately predict residual stresses in a unidirectional carbon fiber/epoxy composite using molecular dynamics and finite element analysis simulation techniques. The results of this work demonstrate that process-induced residual stresses have a significant impact on the composite strength in transverse tension, out-of-plane shear, and in-plane shear, with a maximum reduction in strength of 35%. Moving forward, this method can be used as a design and optimization tool for future composite structures for specific engineering applications and can provide processing parameters that can maximize desirable composite properties and/or minimize composite manufacturing energy and cost.

1. Introduction

Epoxy-based polymer matrix composites (PMCs) are being increasingly used in structural components of modern commercial aircraft because of their excellent specific stiffness and specific strength. During the manufacturing of PMC laminates and structures, cure shrinkage of the epoxy and differential thermal contraction mismatch between the epoxy and fiber reinforcement cause the formation of residual stresses. These residual stresses can cause a loss in product durability and undesired residual deformations [1-8]. Understanding the link between processing conditions and evolution of residual stresses is critical to improve the lifecycle of structural components.

The classical approach to optimizing processing parameters to minimize residual stresses in PMCs is through an experimental-based trial-and-error approach. Parameters such as cure cycle temperatures, hold times, and ramp rates are systematically adjusted to determine the cycle that yields minimal levels of residual stress/deformation. However, such approaches are inefficient and expensive. An alternative approach is through process modeling [9-27], which aims to optimize processing parameters using a combination computational tools and experimental characterization techniques to efficiently establish a set of processing parameters that mitigate the formation of residual stresses.

Previous process modeling efforts [11, 12, 17-22] have utilized finite element analysis (FEA) as the primary computational driver for parameter optimization. Unfortunately, FEA tools are limited to continuum length scales (> 1 μm), and thus cannot capture the physics of material behavior at the molecular level (~ 1 nm). As a result, some process modeling efforts [9, 11, 12, 17-19, 23] have relied on phenomenological relationships to link physical, mechanical, and thermal properties of neat resin to the degree of cure, which is essential information for comprehensive process modeling. However, phenomenological methods do not provide reliable, physics-based properties for a wide range of resins. Therefore, the development of more accurate and comprehensive process modeling techniques will require the incorporation of multi-scale computational modeling that covers both molecular and continuum length scales.

The objective of this study is to establish a new multiscale process modeling method to accurately predict residual stresses in epoxy-based PMCs using molecular dynamics (MD) and FEA simulation techniques. MD is used to predict a complete set of physical and mechanical properties of a bisphenol-A-based epoxy as a function of degree of cure, and the results are validated using a series of material characterization and testing techniques. The MD predictions are subsequently used in FEA simulations to predict the process-induced residual stresses of carbon fiber/epoxy composites and their influence on the composite stiffness and strength. It is shown that the process-induced residual stresses can have a significant impact on composite strength. Thus, this multiscale approach is an effective and efficient tool for optimization of processing parameters for high-performance PMCs.

2. Material

The epoxy resin used in this study is diglycidyl ether of bisphenol A (DGEBA), sold commercially as EPON 828 (Figure 1a). Jeffamine D230, a poly(oxypropylene) diamine (POPD), was used as the curing agent (Figure 1b), where there is an average of 2.5 oxypropylene groups per monomer. The neat epoxy resin was supplied by Hexion Inc., and the curing agent was supplied by Huntsman Corporation. Comprehensive experimental testing and characterization were performed on this resin, including mass density measurements, tensile testing, differential scanning calorimetry (DSC), and dynamic mechanical analysis (DMA). The full details of these tests are included in the Supporting Information.

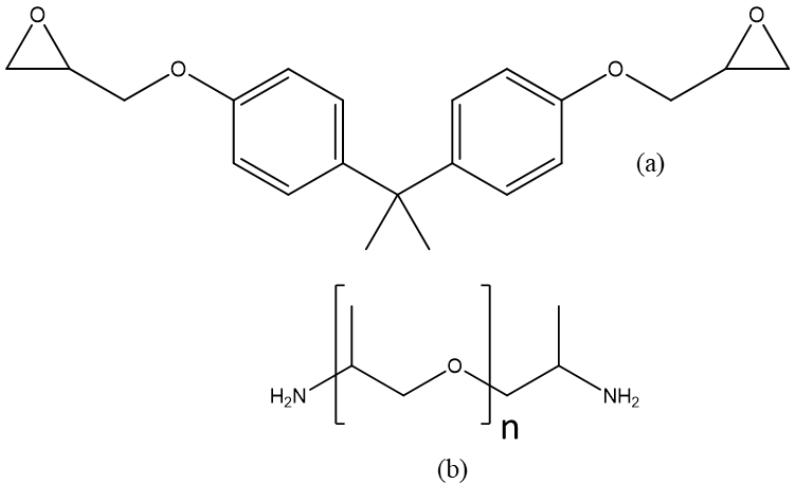

Figure 1. Molecular structures of (a) DGEBA and (b) POPD (n = 2.5).

3. MD modeling

The proposed multiscale modeling approach is depicted in Figure 2. The workflow consists of two subprocesses: Virtual curing and virtual testing. Virtual curing was performed in two steps and occurred at the nano- and micro-scales. MD was used to predict neat resin properties as a function of the degree of cure. Degree of cure is defined as the relative amount of conversion that has occurred in a thermosetting polymer system, ranging from 0 (no crosslinking reactions have occurred) to 1.0 (100% of all crosslinking reactions have occurred that can possibly occur given steric hindrance constraints). The MD predicted properties are used as input in FEA to simulate in-situ curing in the presence of carbon fiber and predict the resulting residual stress. Virtual testing was then performed to predict properties of the composite at the microscale, which was ultimately used to inform higher length-scale analyses.

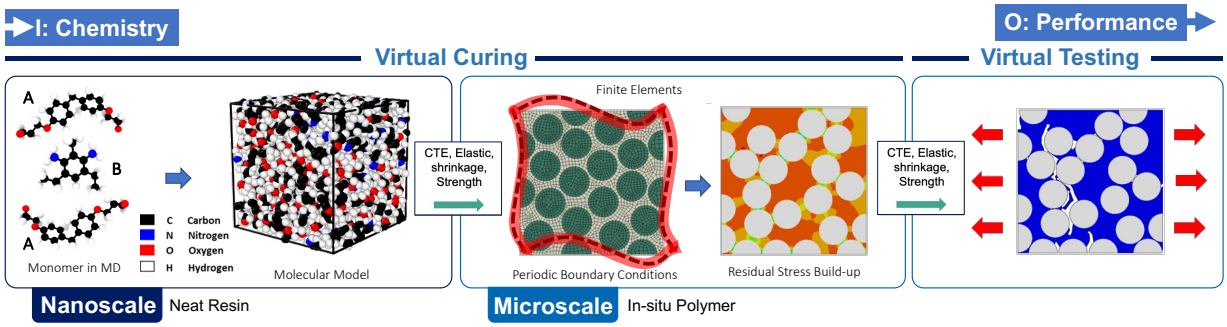

Figure 2. Multiscale approach for process modeling of the carbon fiber/epoxy composite.

3.1 Model set-up

The Large-scale Atomic/Molecular Massively Parallel Simulator (LAMMPS) software package, version June 2018, was used for performing all the MD simulations discussed herein [28]. OVITO was used for all visualizations presented herein [29]. The IFF-R forcefield [30] was used to

simulate the interatomic interactions, which utilizes morse potentials to simulate covalent bond stretching. The morse potential enables the accurate calculation of bond-stretch energies at large deformations, up to the point of bond scission. IFF-R has been validated previously for thermoset resins [31-33]. All the simulations discussed herein were performed using periodic boundary conditions with the Nose-Hoover thermostat and barostat [34-37] with "aniso" settings in LAMMPS. The MD models were constructed, equilibrated, and crosslinked as described in detail in the Supporting Information. To account for statistical variation in the predicted properties, five replicate models were independently built and simulated.

3.2 Physical property predictions

The gel point of the epoxy for each crosslink density and replicate was determined by calculating the molecular mass of the largest molecule (denoted as the "primary chain") and second-largest molecule (denoted as the "secondary chain"), as well as the reduced molecular weight (RMW) of the model [38, 39]. The RMW is the average molecular mass of all the molecules in the system except the primary chain. Figure S6 shows a representative plot of the three metrics which were computed at every degree of cure. The inflection point of the molecular mass of the primary chain curve indicates the gel point of the material, and the peaks of molecular mass of the secondary chain and the RMW are alternative indicators of the gel point. The average predicted gel point was 55.2 ± 5.4 % for the three metrics and five replicates.

The mass density and cure-induced volumetric shrinkage for each degree of cure and replicate were obtained from the MD simulations using time-averaged values over 1 ns. For every model, the shrinkage was computed by comparing the predicted simulation box volume to the uncured (degree of cure = 0) model. Based on the predicted gel point and the volumetric shrinkage data, the post-gelation volume shrinkage was also determined for each crosslinking density above the gel point.

3.3 Mechanical property predictions

To obtain the bulk modulus values as a function of degree of cure, the models were subjected to a hydrostatic pressure of 5000 atm at room temperature using the constant pressure and temperature (NPT) ensemble, and the corresponding volumes were compared to those from the equilibration simulation at 1 atm, as described in detail elsewhere [40]. For the shear modulus values, the simulation boxes were first converted to "triclinic" in LAMMPS and simulated for 500 ps using the NPT ensemble. Shear deformations were performed in the xy, xz and yz planes at room temperature with a strain rate of 2×10^{8} s^{-1}. OriginPro, a statistical analysis tool, was used to analyze the stress-strain data and compute the shear modulus [41].

Young's modulus and Poisson's ratio values were calculated from the predicted bulk and shear moduli at each crosslink density using the linear-elasticity equations for isotropic materials [42]. Odegard et al. [31] explained a detailed procedure to compute the yield strength from shear deformation simulations. The same approach was implemented in this work.

Ideally, MD predictions could be directly used as input polymer properties for the FEA simulations discussed in the following section. However, MD predictions of mechanical properties of polymers

are typically over-predictive because of the visco-elastic nature of these materials and the nanosecond time scales associated with simulated MD deformations [31, 43, 44]. This over-prediction is especially significant for lower degrees of cure and higher temperatures. A correction was applied to the MD predictions to mitigate the so-called strain-rate effect, which is detailed in Section 2.4 of the Supporting Information.

4. FEA modeling

Computational process modeling and mechanical property prediction of composite microstructures was carried out using representative volume elements (RVEs) modeled with the commercial FEA software Abaqus/STANDARD. The details of the RVE generation, process modeling procedure, and property prediction of the RVEs are discussed in the following sub-sections.

4.1 RVE generation

In this study, an RVE size of 50 fibers was chosen based on the statistical size-effect study performed by Shah et al. [45]. Five periodic RVEs were generated comprised of a random dispersion of IM7 carbon fibers (fiber diameter of 6 μm) in the epoxy matrix. The five microstructure renditions (Figure 3) were produced at a fiber volume fraction of 60% with the aid of a random RVE generator developed by Stapleton et al. [46, 47]. Perfect bonding was assumed between the fiber and the matrix. The fibers were modeled as transversely isotropic solids, the thermo-mechanical properties of which are summarized in **Error! Reference source not found.**. The physical, mechanical, and thermal properties of the epoxy determined through MD simulations were assigned to the isotropic matrix material. Each RVE was meshed with C3D8T elements (eight-node brick elements with temperature degrees of freedom). Periodic boundary conditions, as illustrated in Figure 4, were prescribed to the RVEs, the implementations of which can be found elsewhere [16].

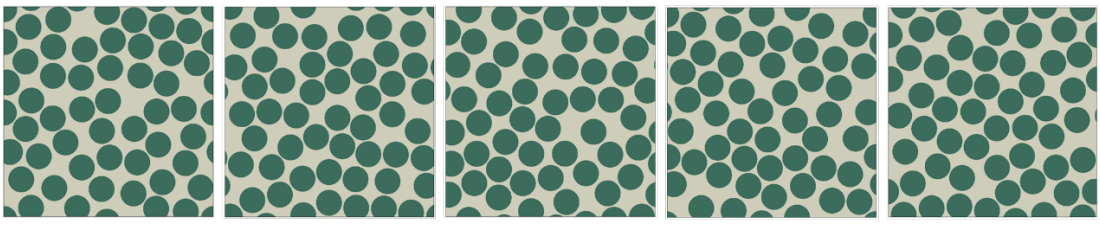

Figure 3. Five distinct realizations of a 50-fiber RVE generated by the random RVE generator

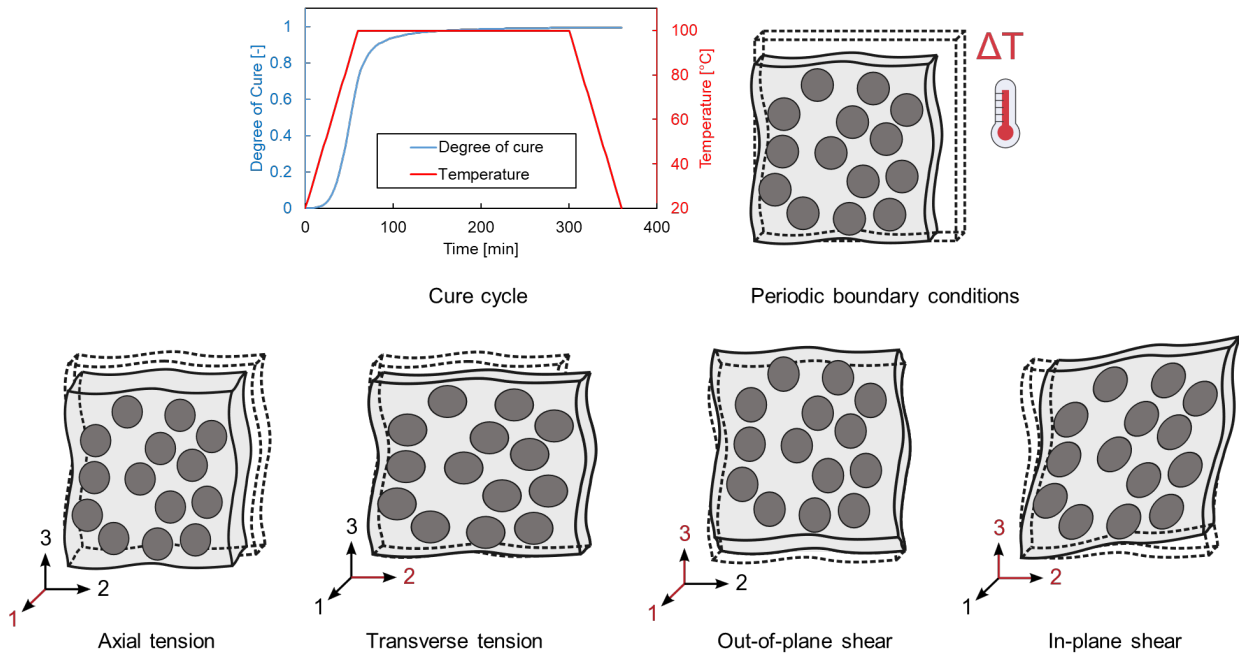

Figure 4. Mechanical and thermal boundary conditions prescribed to the RVEs during virtual curing and mechanical test simulations. The cartesian coordinates indicate axial (1) and transverse (2, 3) directions. The arrows marked in red color indicate the mechanical displacements prescribed for axial, transverse and out-of-plane and in-plane shear loading conditions.

4.2 Process modeling and residual stress prediction

To relate processing conditions with the formation of residual stresses in the simulated RVEs, computational process modeling was performed using the approach developed by Shah et al. [45, 48]. A coupled temperature-displacement analysis was carried out in Abaqus/STANDARD with user-subroutines UMATHT and UMAT. For a prescribed cure cycle (see Figure 4), the Prout-Thompkins kinetic model (Equation (3)) with the kinetic constants provided in **Error! Reference source not found.** was simultaneously solved with a three-dimensional Fourier heat transfer equation to predict the temperature evolution and cure distribution within the RVE. For a given degree of cure and temperature distribution within the RVE, the instantaneous matrix properties from the MD simulation were utilized, and the corresponding residual stresses were predicted [45, 48]. Thus, the accumulation of residual stresses within the RVE was governed by the evolution of the matrix elastic modulus and the chemical and thermal strains induced by the processing.

4.3 Virtual mechanical testing

The virtually-cured RVEs were subjected to a series of simulated deformations to predict their mechanical response as influenced by the process-induced residual stresses. The RVEs were subjected to axial tension, transverse tension, in-plane shear, and out-of-plane shear deformations. A schematic of the prescribed mechanical boundary conditions for each loading case are illustrated in Figure 4. Additionally, RVEs with no residual stresses (as a baseline comparison) were subjected to the aforementioned mechanical deformations to quantify the influence of process-induced residual stresses on their mechanical response. For these analyses, the RVEs were assumed to be initially stress-free and were assigned in-situ matrix properties corresponding to the

fully-cured state. The composite stiffness and strength values for various loading conditions were determined through virtual mechanical testing and compared with the corresponding values of the process-modeled RVEs.

Mechanical failure in the RVEs was modeled with a previously-developed progressive damage model [45] based on Crackband theory [49], as implemented within Abaqus/STANDARD with the UMAT user-written subroutine. Failure was assumed to initiate in elements for which the maximum principal stress exceeded their prescribed strength. A traction-separation law governed by the fracture energy was used to define the post-peak softening behavior, details of which can be found elsewhere [45]. A scalar damage field variable was computed based on this traction-separation law to incrementally degrade the stiffness of the damaged element [45]. Failure was admissible in the fibers only for the axial tension case when the maximum principal stresses exceeded the fiber tensile strength. The fiber failure was assumed to be brittle, thus no post-peak softening behavior was modeled for the axial loading cases. For all other loading cases, which induced failure in the matrix, fibers were modeled as transversely isotropic linear-elastic solids. The in-situ matrix was assumed to fail in mode I when the maximum principal stresses in the matrix exceeded the critical tensile and shear strengths during transverse tension and shear loading conditions, respectively. This assumption was confirmed by the work of Pineda et al. [50] where mixed mode failure (mode I and mode II) was enabled for the in-situ matrix subjected to shear loading conditions. However, the matrix manifested only mode I failure. The in-situ matrix was prescribed a critical tensile strength $\sigma_t = 64.5$ MPa, shear strength $\sigma_{sh} = 50$ MPa, and mode I fracture energy $G_{IC} = 0.001$ J/m^2.

5. Results and discussion

5.1 Molecular Dynamics

Figure 5a shows the mass density predictions for all the models as a function of the degree of cure at 27 °C, as well as experimental values from the density measurements described above and the literature [51-53]. For the fully polymerized models, the MD predicted density is 1.153 ± 0.002 g/cm^3. The plot in Figure 5a shows a linear trend below the gel point, with a plateauing of the curve above the gel point. Near the gel point, the network connects all of the monomers with strong covalent bonds and thus the complete network resists further change in the volume. The predicted values show an excellent match with the experimental values and with the available values from the literature. In comparison to previous MD studies [54-57], the predicted densities show closer agreement with experiments, which is a critical factor for accurate prediction of polymer thermal mechanical properties [31, 58].

Figure 5b shows the volumetric shrinkage as a function of the degree of cure. Similar to the mass density, there is nearly a linear relationship up to the gel point, with no further shrinkage occurring after the gel point. The predicted total shrinkage for the fully crosslinked state at 27 °C is 1.63 ± 0.34 %. Figure 5b also shows the predicted post-gelation shrinkage (relative shrinkage after the gel point), with a generally increasing trend. The post-gelation shrinkage predicted for the maximum crosslinked model was 0.43 ± 0.35 %.

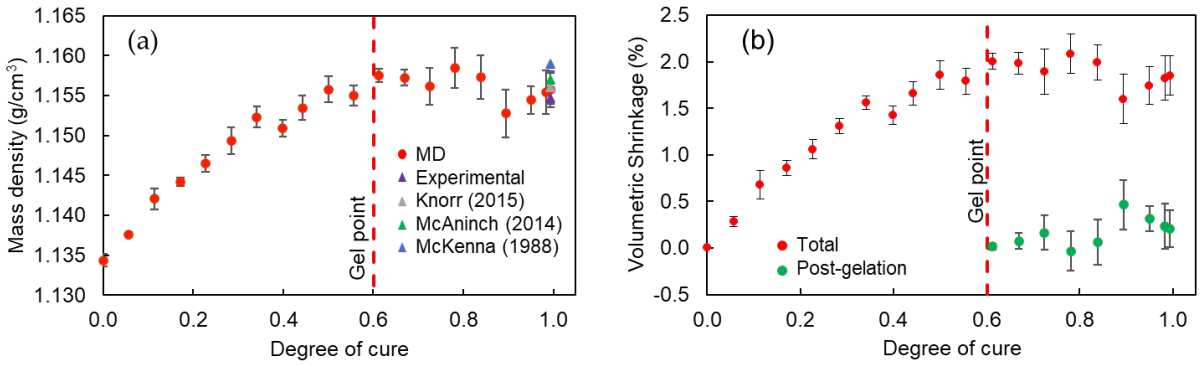

Figure 5. Physical property predictions with comparison to experiment: (a) Mass density and (b) volumetric shrinkage. The error bars in all the associated graphs represent the standard deviation of the five simulated replicates.

Figure 6a shows the predicted Young's modulus as a function of degree of cure. The Young's modulus clearly shows a sigmoidal increase with increasing degree of cure through the point of gelation. In the fully-crosslinked state, the predicted Young's modulus is 3.33 GPa and the experimentally-measured value from tensile testing is 2.67 ± 0.04 GPa. Comparison of the predicted values, measured values, and values from the literature [51, 59-61] indicates reasonable agreement between modeling and experiment at the fully crosslinked state, thus validating the modeling approach.

Figure 6b shows the Poisson's ratio prediction as a function of degree of cure. In general, the Poisson's ratio shows a nearly linear decrease with increasing crosslink density. The predicted value for the fully crosslinked state after applying the viscous correction is 0.41. The experimental measurements from the tensile testing indicate a value of 0.38 ± 0.01, which is very close to the predicted value. At 0% crosslink density, the predicted value is 0.5. For many liquids, the Poisson's ratio is close to 0.50 [62], thus validating the prediction for 0% crosslink density.

6.5

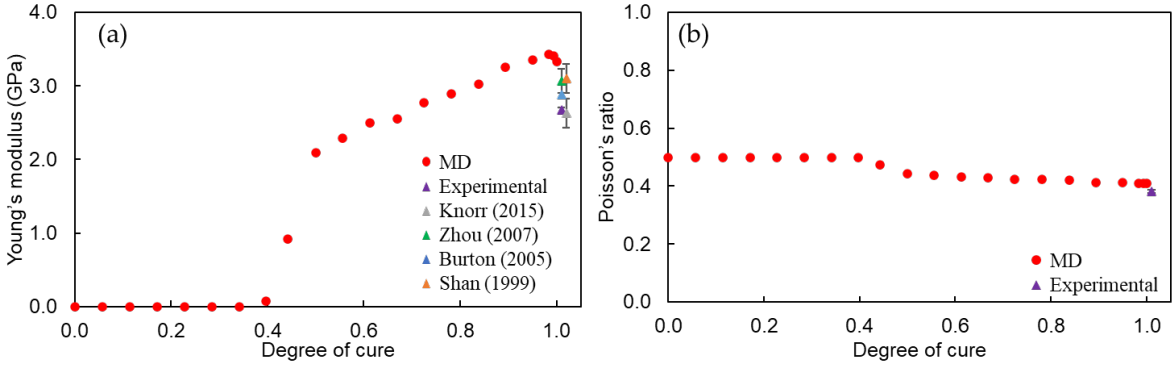

Figure 6. Mechanical property predictions with comparison to experiment: (a) Young's modulus, and (b) Poisson's ratio. The error bars in all the associated graphs represent the standard deviation of the five simulated replicates.

5.2 Finite element analysis

The representative end-of-cure residual stress contour plot (maximum principal stress) is presented in Figure 7c. The stresses in the in-situ matrix were predominantly tensile in nature. Due to the

random fiber distribution, the RVE exhibited regions with high stress concentrations which became potential failure sites during subsequent mechanical loading. Such sites are evident in Figure 7c marked with warmer colors (yellow to red). Each RVE subjected to the process modeling analysis had a unique fiber packing topology. As a result, the spatial distribution of residual stresses within the RVE varied considerably. However, each RVE registered a very consistent maximum and volume-averaged end-of-cure residual stress of 30 $\pm$ 0.8 MPa and 9.6 $\pm$ 0.2 MPa, respectively.

5.2.1 Transverse tension

Figure 7a shows the global transverse stress σ_{22} versus strain ϵ_{22} plot of a representative microstructure subjected to a displacement in the transverse direction (u_2). An initial linear-elastic response was observed as the RVE was loaded transversely. Following the linear regime, a pre-peak non-linearity was observed. At this point, the stresses in resin-rich regions of the RVE approached the critical load-carrying capacity in the presence of fiber-induced stress concentrations. The corresponding local failure and microcracking within the RVE manifested itself as a change in the slope of the global stress-strain response. Following this failure initiation, the global stresses in the RVE dropped to zero as the local microcracks coalesced into a large crack which propagated along the path of least resistance (or highest stress concentration), resulting in catastrophic failure of the RVE. Figure 7d shows the contour plot of the damage field variable which illustrates the crack path in the RVE due to transverse mechanical loading. An average transverse composite stiffness E_{22}^{+} = 9468 $\pm$ 85 MPa and strength S_{22}^{+} = 26 $\pm$ 0.6 MPa was predicted for the five RVEs.

To ensure transverse isotropy, the same set of RVEs were subjected to transverse displacements u_3, and their global transverse stress σ_{33} versus strain ϵ_{33} response was predicted. A similar response was observed relative to the u_2 displacement where the RVE exhibited an initial linear elastic response followed by a pre-peak non-linearity before final failure (see Figure 7a). The crack path, shown in Figure 7e, passed through regions of densely packed fibers with relatively high stress concentrations. Comparable average stiffness and strength values as with the u_2 displacement case was predicted: E_{33}^{+} = 9456 $\pm$ 85 MPa and S_{33}^{+} = 26 $\pm$ 0.7 MPa. Thus, the simulated microstructure can be considered as transversely isotropic.

5.2.2 Out-of-plane shear

The global shear stress σ_{13} versus shear strain ϵ_{13} plot for a representative microstructure subjected to displacements u_1 and u_3 is presented in Figure 7a. Similar to the transverse tension loading cases, the linear elastic region is followed by non-linearity resulting from local microcracking. A final drop in the global out-of-plane shear stresses corresponded to a catastrophic failure of the RVE. Local cracking can be observed at several locations in the RVE (see Figure 7g) which then resulted in a large crack. The predicted average stiffness and strength were E_{13} = 4997 $\pm$ 61 MPa and S_{13} = 21 $\pm$ 1.1 MPa, respectively.

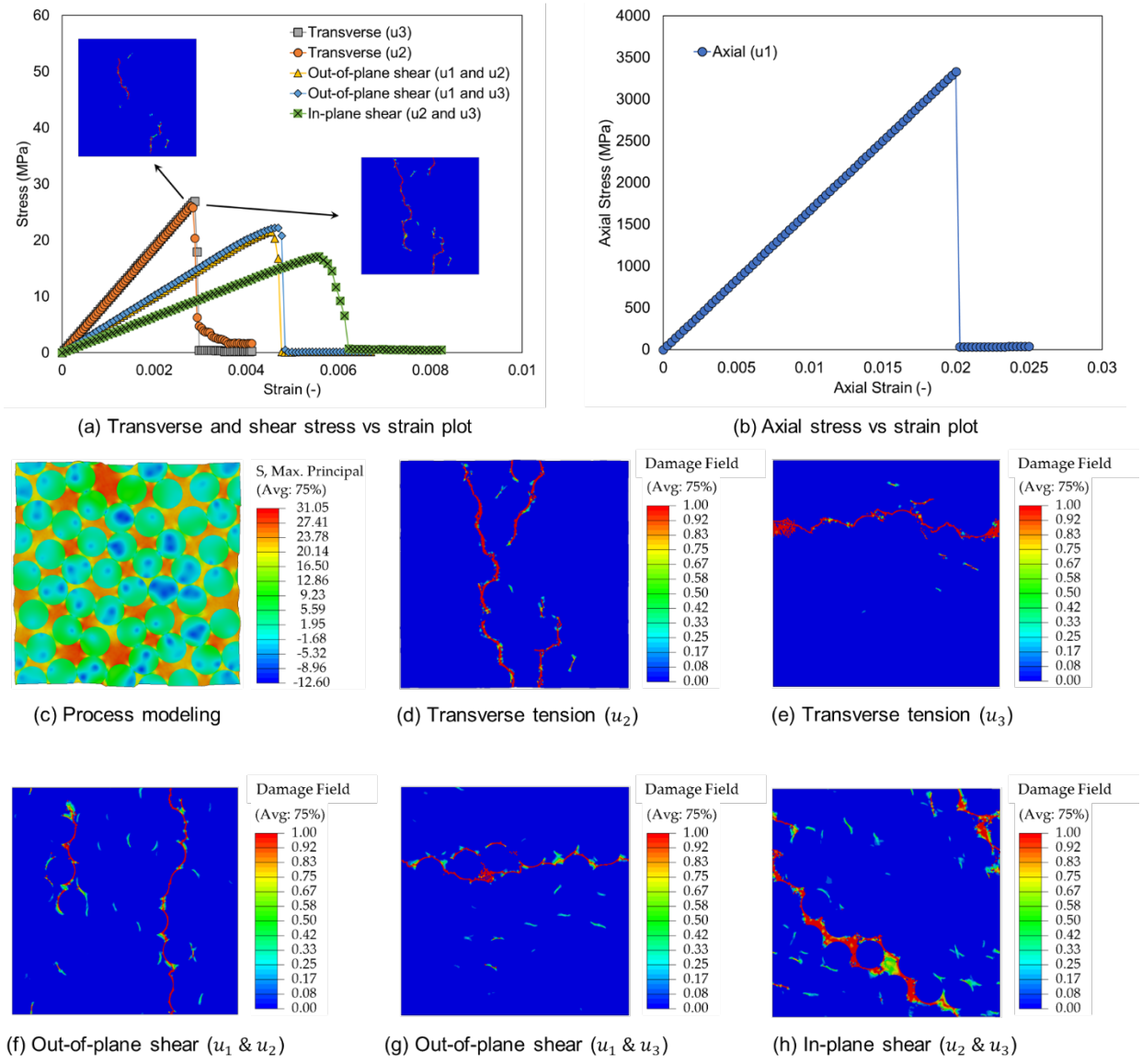

(a) Transverse and shear stress vs strain plot

(b) Axial stress vs strain plot

(c) Process modeling

(d) Transverse tension (u_2)

(e) Transverse tension (u_3)

(f) Out-of-plane shear (u_1 & u_2)

(g) Out-of-plane shear (u_1 & u_3)

(h) In-plane shear (u_2 & u_3)

Figure 7. Stress versus strain plots of the representative microstructure when subjected to (a) transverse and shear loads and (b) axial loads; contour plots of (c) end-of-cure residual stress (maximum principal), and damage field variable during (d) transverse tension displacements u_2, (e) transverse tension displacements u_3, (f) out-of-plane shear displacements u_1 and u_2, (g) out-of-plane shear displacements u_1 and u_3, and (f) in-plane shear displacements u_2 and u_3.

Similar trends were observed when the RVEs were subjected to out-of-plane shear displacements u_1 and u_2. The global shear stress σ_{12} versus strain ϵ_{12} response and the final damage field variable contour plot can be seen in Figure 7a and Figure 7f, respectively. As expected, the RVEs registered very comparable stiffness and strength values of $E_{12} = 5035 \pm 53$ MPa and $S_{13} = 22 \pm 0.7$ MPa, respectively, ensuring the transversely isotropic response of the composites.

5.2.3 In-plane shear

The in-plane shear stress σ_{23} versus shear strain ϵ_{23} plot exhibits a similar behavior as the out-of-plane shear except with lower stiffness and strength values of E_{23} = 3152 $\pm$ 38 MPa and S_{23} = 18 $\pm$ 0.6 MPa. As shown in Figure 7h, this deformation mode induced the formation of a relatively high number of angular microcracks. At the ultimate shear stress, a single angular crack band formed from the coalescence of these angular microcracks.

5.2.4 Axial tension

The axial stress σ_{11} versus axial strain ϵ_{11} response of the representative RVE subjected to a global strain along the fiber direction is presented in Figure 7b. The RVE exhibited a linear response up to the failure stress. After the ultimate stress was achieved, the global stress in the RVE dropped suddenly to zero suggesting that the load-carrying capacity of the RVE had completely diminished with the failure of the fibers. Axial stiffness E_{11}^{+} = 167 GPa and an axial strength S_{11}^{+} = 3 GPa values were predicted (standard deviations were negligible). The axial response of the RVEs showed a negligible dependence on the random fiber packing.

5.2.5 Significance of process-induced residual stresses

A comparison of the stiffness and strength values of the composite including and excluding the process-induced residual stresses is provided in Figure 8. A negligible difference (< 2%) was observed in the composite stiffness predictions with residual stresses, suggesting that process-induced residual stresses have a negligible influence on composite stiffness values. By contrast, a significant difference was observed in the matrix-dominated composite strength predictions. Specifically, the transverse composite strengths S_{22}^{+} and S_{22}^{+} were overestimated by 16.5% and 20.5%, respectively, when residual stresses were not considered. Similarly, the out-of-plane shear strengths S_{12} and S_{13} were overestimated by ~30% when residual stresses were ignored. The in-plane shear strength exhibited a significant difference of 35%. On the contrary, the fiber-dominated strength S_{11}^{+} exhibited a negligible difference of 0.01%. These trends clearly suggest that process-induced residual stresses significantly influence the matrix-dominated composite strength.

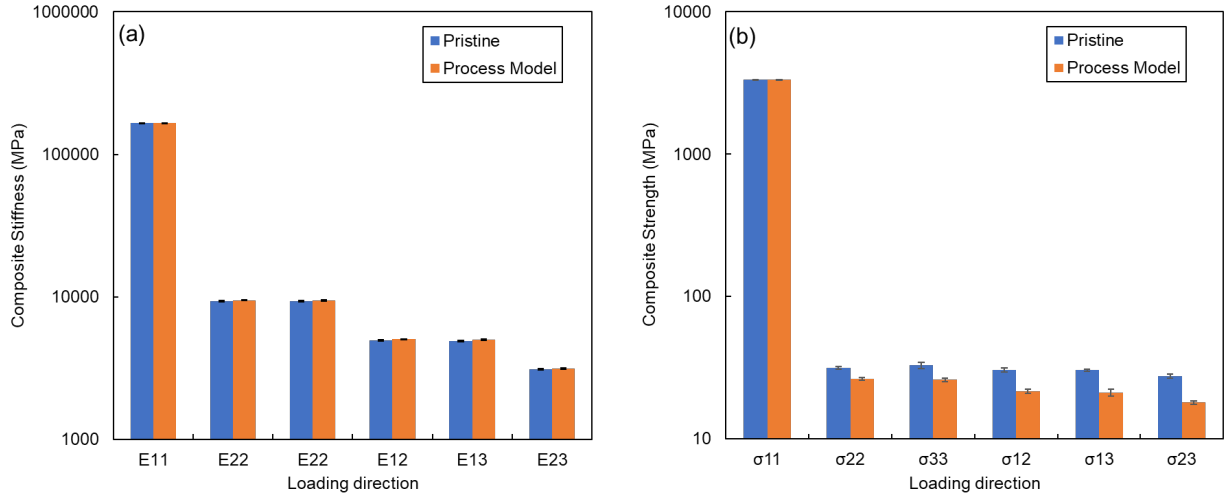

Figure 8. (a) Composite stiffness and (b) strength prediction summary for simulations that include and exclude process-induced residual stresses

6. Conclusion

The results of the multiscale process modeling discussed herein demonstrate an important point: Process-induced residual stresses have a significant impact on matrix-dominated unidirectional PMC strength values. Specifically, the transverse tension, out-of-plane shear, and in-plane shear deformation strength values were reduced by up to 35% with the inclusion of process-induced residual stresses. Therefore, it follows that multiscale computational process modeling is necessary for the accurate prediction of PMC strength allowables in composite structural design.

The predictive power and efficiency of this multiscale process modeling approach can be used as a design and optimization tool for future PMC designs for specific engineering requirements. Starting with molecular-level information that provides property vs degree of cure information, processing parameters can be adjusted in the FEA framework to minimize process-induced residual stresses and maximize the corresponding composite strength allowables. Such optimization not only provides processing parameters that maximize desirable composite properties, but can also provide processing parameters that minimize PMC manufacturing energy and cost.

Acknowledgements

This research was partially supported by the NASA Space Technology Research Institute (STRI) for Ultra-Strong Composites by Computational Design (US-COMP), grant NNX17AJ32G; and NASA grants 80NSSC19K1246 and 80NSSC21M0104. SUPERIOR, a high-performance computing cluster at Michigan Technological University, was used in obtaining the MD simulation results presented in this publication.

Competing interests

The authors declare no competing financial or non-financial interests

Data availability

All data generated and/or analyzed during this study are included in this article

Author contributions

Prathamesh Deshpande: Conceptualization, data curation, formal analysis, investigation, methodology, visualization, writing – original draft, writing - review & editing
Michael Olaya: Conceptualization, data curation, formal analysis, investigation, methodology, visualization, writing – original draft, writing - review & editing
Aaron Krieg: Investigation, methodology, validation, writing – original draft, writing – review & editing
Sagar Patil: Conceptualization, data curation, formal analysis, investigation, methodology, visualization, writing – original draft, writing – review & editing

Sagar Shah: Conceptualization, data curation, formal analysis, investigation, methodology, visualization, writing – original draft, writing – review & editing
Julia King: Methodology, supervision, writing – review & editing
Gregory Odegard: Conceptualization, formal analysis, funding acquisition, methodology, project administration, resources, supervision, writing - review & editing
Marianna Maiaru: Conceptualization, formal analysis, funding acquisition, methodology, project administration, resources, supervision, writing - review & editing

References

1. Plepys, A.R. and R.J. Farris, *Evolution of residual stresses in three-dimensionally constrained epoxy resins.* Polymer, 1990. **31**(10): p. 1932-1936.
2. Baran, I., et al., *A review on the mechanical modeling of composite manufacturing processes.* Archives of computational methods in engineering, 2017. **24**(2): p. 365-395.
3. Chekanov, Y.A., et al., *Cure shrinkage defects in epoxy resins.* Polymer, 1995. **36**(10): p. 2013-2017.
4. Benedikt, B., et al., *An analysis of residual thermal stresses in a unidirectional graphite/PMR-15 composite based on X-ray diffraction measurements.* Composites Science and Technology, 2001. **61**(14): p. 1977-1994.
5. Hyer, M.W., *Some Observations on the Cured Shape of Thin Unsymmetric Laminates.* Journal of Composite Materials, 1981. **15**(2): p. 175-194.
6. Hyer, M.W., *Calculations of the Room-Temperature Shapes of Unsymmetric Laminatestwo.* Journal of Composite Materials, 1981. **15**(4): p. 296-310.
7. Hyer, M.W., *The Room-Temperature Shapes of Four-Layer Unsymmetric Cross-Ply Laminates.* Journal of Composite Materials, 1982. **16**(4): p. 318-340.
8. Maiaru, M., *Effect of uncertainty in matrix fracture properties on the transverse strength of fiber reinforced polymer matrix composites*, in *2018 AIAA/ASCE/AHS/ASC Structures, Structural Dynamics, and Materials Conference*. 2018, American Institute of Aeronautics and Astronautics.
9. White, S.R. and H.T. Hahn, *Process Modeling of Composite Materials: Residual Stress Development during Cure. Part I. Model Formulation.* Journal of Composite Materials, 1992. **26**(16): p. 2402-2422.
10. White, S.R. and H.T. Hahn, *Process Modeling of Composite Materials: Residual Stress Development during Cure. Part II. Experimental Validation.* Journal of Composite Materials, 1992. **26**(16): p. 2423-2453.
11. Danzi, F., et al., *A numerical micro-mechanical study on damage induced by the curing process in carbon/epoxy unidirectional material.* Composite Structures, 2019. **210**: p. 755-766.
12. Hui, X., et al., *Microscale viscoplastic analysis of unidirectional CFRP composites under the influence of curing process.* Composite Structures, 2021. **266**: p. 113786.
13. D'Mello, R.J. and A.M. Waas, *Virtual curing of textile polymer matrix composites.* Composite Structures, 2017. **178**: p. 455-466.
14. D'Mello, R.J., M. Maiaru, and A.M. Waas, *Effect of the curing process on the transverse tensile strength of fiber-reinforced polymer matrix lamina using micromechanics computations.* Integrating Materials and Manufacturing Innovation, 2015. **4**(1).

15. D'Mello, R.J., M. Maiaru, and A.M. Waas, *Virtual manufacturing of composite aerostructures.* Aeronautical Journal, 2016. **120**(1223): p. 61-81.
16. Maiaru, M., R.J. D'Mello, and A.M. Waas, *Characterization of intralaminar strengths of virtually cured polymer matrix composites.* Composites Part B-Engineering, 2018. **149**: p. 285-295.
17. Rabearison, N., C. Jochum, and J.C. Grandidier, *A FEM coupling model for properties prediction during the curing of an epoxy matrix.* Computational Materials Science, 2009. **45**(3): p. 715-724.
18. Hu, H., et al., *Investigation of non-uniform gelation effects on residual stresses of thick laminates based on tailed FBG sensor.* Composite Structures, 2018. **202**: p. 1361-1372.
19. Hui, X., Y. Xu, and W. Zhang, *An integrated modeling of the curing process and transverse tensile damage of unidirectional CFRP composites.* Composite Structures, 2021. **263**: p. 113681.
20. Yang, L., et al., *Effects of inter-fiber spacing and thermal residual stress on transverse failure of fiber-reinforced polymer–matrix composites.* Computational Materials Science, 2013. **68**: p. 255-262.
21. Zhao, L.G., N.A. Warrior, and A.C. Long, *A micromechanical study of residual stress and its effect on transverse failure in polymer–matrix composites.* International Journal of Solids and Structures, 2006. **43**(18): p. 5449-5467.
22. Shah, S.P. and M. Maiarù, *Effect of Manufacturing on the Transverse Response of Polymer Matrix Composites.* Polymers, 2021. **13**(15): p. 2491.
23. Zobeiry, N., R. Vaziri, and A. Poursartip, *Computationally efficient pseudo-viscoelastic models for evaluation of residual stresses in thermoset polymer composites during cure.* Composites Part A: Applied Science and Manufacturing, 2010. **41**(2): p. 247-256.
24. D'Mello, R.J., et al., *Integrated Computational Modeling for Efficient Material and Process Design for Composite Aerospace Structures*, in *AIAA Scitech 2020 Forum*. 2020, American Institute of Aeronautics and Astronautics.
25. Patil, S., et al., *Multi-Scale Approach To Predict Cure-Induced Residual Stresses In An Epoxy System*, in *35th American Society for Composites Conference*. 2020: Jersey City, NJ.
26. Shah, S., et al., *Multiscale Modeling for Virtual Manufacturing of Thermoset Composites*, in *AIAA SciTech Conference*. 2020, American Institute of Aeronautics and Astronautics: Orlando, FL.
27. Shah, S. and M. Maiaru. *Microscale Analysis of Virtually Cured Polymer Matrix Composites Accounting for Uncertainty in Matrix Properties During Manufacturing*. in *33rd Technical Conference of the American Society of Composites*. 2018. Seattle, WA: American Society of Composites.
28. Plimpton, S., *Fast Parallel Algorithms for Short-Range Molecular-Dynamics* Journal of Computational Physics, 1995. **117**(1): p. 1-19.
29. Stukowski, A., *Visualization and analysis of atomistic simulation data with OVITO-the Open Visualization Tool.* Modelling and Simulation in Materials Science and Engineering, 2010. **18**(1).
30. Winetrout, J.J., et al. *Implementing Reactivity in Molecular Dynamics Simulations with the Interface Force Field (IFF-R) and Other Harmonic Force Fields*. 2021. arXiv:2107.14418.

31. Odegard, G.M., et al., *Molecular Dynamics Modeling of Epoxy Resins Using the Reactive Interface Force Field.* Macromolecules, 2021. **54**(21): p. 9815-9824.
32. Patil, S.U., et al., *Reactive Molecular Dynamics Simulation of Epoxy for the Full Cross-Linking Process.* ACS Applied Polymer Materials, 2021. **3**(11): p. 5788-5797.
33. Gaikwad, P.S., et al., *Understanding the Origin of the Low Cure Shrinkage of Polybenzoxazine Resin by Computational Simulation.* ACS Applied Polymer Materials, 2021. **3**(12): p. 6407-6415.
34. Parrinello, M. and A. Rahman, *Polymorphic Transitions in Single-Crystals - a New Molecular-Dynamics Method.* Journal of Applied Physics, 1981. **52**(12): p. 7182-7190.
35. Martyna, G.J., D.J. Tobias, and M.L. Klein, *Constant pressure molecular dynamics algorithms.* The Journal of Chemical Physics, 1994. **101**(5): p. 4177-4189.
36. Tuckerman, M.E., et al., *A Liouville-operator derived measure-preserving integrator for molecular dynamics simulations in the isothermal–isobaric ensemble.* Journal of Physics A: Mathematical and General, 2006. **39**(19): p. 5629-5651.
37. Shinoda, W., M. Shiga, and M. Mikami, *Rapid estimation of elastic constants by molecular dynamics simulation under constant stress.* Physical Review B, 2004. **69**(13): p. 134103.
38. Hadicke, E. and H. Stutz, *Comparison of the structure of step-growth networks obtained by Monte Carlo simulation and branching theory.* Journal of Applied Polymer Science, 2002. **85**(5): p. 929-935.
39. Varshney, V., et al., *A Molecular Dynamics Study of Epoxy Based Networks: Cross-linking Procedure and Prediction of Molecular and Material Properties.* Macromolecules, 2008. **41**(18): p. 6837-6842.
40. Tack, J.L. and D.M. Ford, *Thermodynamic and mechanical properties of epoxy resin DGEBF crosslinked with DETDA by molecular dynamics.* J Mol Graph Model, 2008. **26**(8): p. 1269-75.
41. OriginPro. 2020b, OriginLab Corporation: Northampton, MA, USA.
42. Malvern, L.E., *Introduction to the Mechanics of a Continuous Medium*. 1969, Upper Saddle River, NJ: Prentice-Hall, Inc.
43. Radue, M.S., et al., *Comparing the mechanical response of di-, tri-, and tetra-functional resin epoxies with reactive molecular dynamics.* Journal of Polymer Science Part B-Polymer Physics, 2018. **56**(3): p. 255-264.
44. Odegard, G.M., et al., *Predicting mechanical response of crosslinked epoxy using ReaxFF.* Chemical Physics Letters, 2014. **591**: p. 175-178.
45. Shah, S.P. and M. Maiarù, *Effect of Manufacturing on the Transverse Response of Polymer Matrix Composites.* Polymers, 2021. **13**(15).
46. Husseini, J.F., S.E. Stapleton, and E.J. Pineda. *Artificial Generation of 2-D Fiber Reinforced Composite Microstructures with Statistically Equivalent Features*. in *Proceedings of the American Society for Composites—Thirty-Sixth Technical Conference on Composite Materials*. 2021.
47. Stapleton, S.E., et al., *Representative volume element for parallel fiber bundles: Model and size convergence.* Composites Part A: Applied Science and Manufacturing, 2016. **87**: p. 170-185.
48. Shah, S.P., et al., *Process modeling and characterization of thermoset composites for residual stress prediction.* Mechanics of Advanced Materials and Structures, 2021: p. 1-12.

49. Bažant, Z.P. and B.H. Oh, *Crack band theory for fracture of concrete.* Matériaux et Construction, 1983. **16**(3): p. 155-177.
50. Pineda, E.J., et al., *Progressive failure of a unidirectional fiber-reinforced composite using the method of cells: Discretization objective computational results.* International Journal of Solids and Structures, 2013. **50**(9): p. 1203-1216.
51. Knorr, D.B., et al., *Overcoming the structural versus energy dissipation trade-off in highly crosslinked polymer networks: Ultrahigh strain rate response in polydicyclopentadiene.* Composites Science and Technology, 2015. **114**: p. 17-25.
52. McAninch, I.M., *Molecular Toughening of Epoxy Networks*, in *Chemical Engineering*. 2014, Drexel University: Philadelphia, PA. p. 259.
53. Lee, A. and G.B. McKenna, *Effect of crosslink density on physical ageing of epoxy networks.* Polymer, 1988. **29**(10): p. 1812-1817.
54. Fan, J., et al., *Molecular dynamics predictions of thermomechanical properties of an epoxy thermosetting polymer.* Polymer, 2020. **196**.
55. Masoumi, S., B. Arab, and H. Valipour, *A study of thermo-mechanical properties of the cross-linked epoxy: An atomistic simulation.* Polymer, 2015. **70**: p. 351-360.
56. Sirk, T.W., et al., *High strain rate mechanical properties of a cross-linked epoxy across the glass transition.* Polymer, 2013. **54**(26): p. 7048-7057.
57. Park, H. and M. Cho, *A multiscale framework for the elasto-plastic constitutive equations of crosslinked epoxy polymers considering the effects of temperature, strain rate, hydrostatic pressure, and crosslinking density.* Journal of the Mechanics and Physics of Solids, 2020. **142**.
58. Odegard, G.M., Patil, S. U., Gaikwad, P. S., Deshpande, P. P., Krieg, A. S., Shah, S. P., Reyes, A., Dickens, T., King, J. A., Maiaru, M., *Accurate predictions of thermoset resin glass transition temperatures from all-atom molecular dynamics simulation.* Soft Matter, 2022.
59. Shan, L., *Effect of network structure of epoxy DGEBA-poly (oxypropylene) diamines on tensile behavior.* Journal of polymer science., 1999. **37**(19): p. 2815.
60. Zhou, G., S. Movva, and L.J. Lee, *Nanoclay and long-fiber-reinforced composites based on epoxy and phenolic resins.* Journal of Applied Polymer Science, 2008. **108**(6): p. 3720-3726.
61. Bruce Burton, D.A., Howard Klein, Angela Garibay-Vasquez, Alan Pekarik, Chris Henkee, *Epoxy Formulations Using Jeffamine Polyetheramines*. 2005, Huntsman Corporation: USA. p. 103.
62. Greaves, G.N., et al., *Poisson's ratio and modern materials.* Nature Materials, 2011. **10**(11): p. 823-837.